Droplet deposition in radial turbines

Sebastian Schuster[1]*, Friedrich-Karl Benra[1], Dieter Brillert[1]

ISROMAC 2016

International Symposium on Transport Phenomena and Dynamics of Rotating Machinery

Hawaii, Honolulu

April 10-15, 2016

Abstract

In this paper droplet deposition in radial turbines used for waste heat recovery in the chemical industry is investigated. During expansion, the water vapour in the working fluid undergoes sub-cooling, at a certain point a cloud of fine droplets begins to form and a fraction of these droplets is deposited on the blade surfaces. In this paper, droplet deposition is calculated by incorporating turbulent fluctuations and Brownian motion into a Lagrange particle tracking algorithm. After introducing the calculation approach, a validation of the enhanced CFD code by means of deposition experiments in a straight tube is presented. For a radial turbine, the functional relation between the location of maximum sub-cooling and the onset of droplet deposition is pointed out. Even though the validation of the numerical code is quite satisfactory, some uncertainties arise from the nucleation modelling. This uncertainty will be addressed in the publication as well. The paper concludes with suggestions on how to increase the reliability of the calculations.

Keywords

Condensation, radial turbine, droplet deposition

[1]*Chair of Turbomachinery, University of Duisburg-Essen, Duisburg, Germany*

***Corresponding author**: sebastian.schuster@stud.uni-due.de

INTRODUCTION

At the end of many procedures in the process industry, a gas mixture at high pressure containing water and steam is present. The exergy stored in such mixtures can be converted into mechanical work by using a radial turbine. Condensation may occur during expansion, but before noticeable condensation emerges, sub-cooling of around 20 °C is necessary. Once a cloud of fine droplets has formed, the droplets rapidly grow to a few micrometers. Directly after the fog forms, a part of the fine droplets is deposited on the surface of the blade, mainly by Brownian motion. With increasing droplet diameter, the dominant deposition mechanism changes from Brownian motion to turbulent migration, and finally to inertia-moderated motion.

Condensation in turbo machines has been investigated since the beginning of the 20th century, starting with the work of Baumann [1]. In the mid-20th century, Gyarmathy [2] developed the first theory of the condensation process in axial steam turbines. A fundamental element of this theory is the size of the droplets. This is calculated from the initial size at the birth of the droplets and with a growth law. Bakhtar et al. [3] provide an overview of nucleation models. Different numerical methods can be used to calculate the gas-liquid flow: These are the fully Euler methods; the mixed Euler-Lagrange methods; and the quadrature methods of moments (QMOM). A comprehensive comparison of these methods can be found in White [4].

Yau and Young [5], as well as Young and Yau [6], investigate droplet deposition in axial turbo machines. Crane [7], Starzmann et al. [8], and Starzmann, Casey and Mayer [9] show investigations of droplet deposition in axial steam turbines. These investigations focus on the amount of water deposited and the comparison between two calculation approaches. In one calculation approach the deposition rate is calculated only taking into account the inertia force on a curved stream line. In the other calculation approach the turbulent fluctuation is incorporated as well.

Guha [10] offers a review on deposition calculation and the equations presented are used in this paper. An important conclusion of the work of Young, Yau, and Walters [11] is that the theory of droplet deposition and experiments are consistent. Discrepancies in older publications are explained by an averaged diameter being used for calculation instead of a diameter spectrum. Therefore, in this publication, the Euler-Lagrange method is used for the calculation of the gas-liquid flow, as it can easily handle a diameter spectrum.

Once a droplet hits a wall an interaction with the wall has to be accounted for. This interaction is investigated by Gomaa and Weigand [12] as well as by Schmehl et al. [13]. Their correlation allows the calculation of the behaviour of a droplet when it hits a surface. From these investigations, it can be deduced that very small droplets — barely larger than a micrometer — form a liquid film on the surface of the blade. In the presented case, where the temperature is below saturation temperature and the Weber number is quite small, all droplets dissolve in a liquid film at the surface.

The liquid film motion is mainly influenced by the wall-shear stress and the centrifugal force. Even at an assumed film thickness of a micrometer, the direction of motion is mainly radially outward oriented (Schuster et al. [14]). Such thin films have never been measured in applications related to turbomachines and it is likely that the film is thicker as it breaks up into rivulets. While the film gets thicker, the centrifugal force becomes even more dominant. Droplets originating from the water films might cause damage to the turbine and that is the reason why investigating droplet deposition in radial turbines is necessary.

In this paper the functional relationship between the location of maximum sub-cooling and deposition onset is determined. Whereas, in axial steam turbines, the amount of water is important to calculate the erosion rate, in radial

turbines, the location of deposition onset is the key factor to determine liquid film motion.

Because the focus of investigations has not been before on the onset of deposition, the nucleation model used is investigated for parameters having an influence on the results.

1. METHOD

1.1 Condensation

The calculation of the gas phase is based on the Reynolds-averaged Navier-Stokes equations in integral form. With the *k-ω* SST turbulence model purposed by Menter [15], the system of equations is closed. This results in seven partial differential equations which are transformed into an algebraic system of equations by applying the finite volume method on a block-structured mesh. Due to nucleation droplets begin to form, and their motion is calculated in consideration of Newton's second law. Interaction between the gas phase and the droplets is calculated by the particle-source-in-cell method [16]. In each finite volume, the number of droplets formed by nucleation is calculated. Once the calculated number n_{dr} is above a predetermined nucleation rate threshold value of NRT = 1.0 x 10^{+15} 1/(m³·s), a particle path consisting of n_{dr} droplets is initialised in the finite volume. All particle paths exchange mass, momentum, and energy with the surrounding gas phase. Therefore, the calculation of the two sets of equations is conducted one after another until a converged solution for both systems is obtained. This approach is often called two-way coupling. The number of droplets formed is calculated with classical nucleation theory and the droplet growth using heat and mass transfer models. A large number of publications are available on condensation models [14], [17–24]. The one used here is described in Schuster et al. [14]. The empirical factors in the models are set to: q_c = 1.0, ν = 0.0, NBTF = 0.975. Schuster et al. [14] also perform a validation of the code. Therefore, the flow in a Laval nozzle is calculated and static pressure along the nozzle axis as well as droplet diameter at one point on the nozzle axis are compared to the experimental results. A general good agreement between measured and calculated values is obtained in terms of static pressure. A larger deviation exists for the droplet diameter but is still in the same magnitude. A discussion and conclusions related to the discrepancy and empirical factors are given by Schuster et al. [14] [24].

1.2 Droplet transport and droplet deposition

The droplet trajectory results from both the droplet origin and the forces acting on the droplet. Droplets are tracked in consideration of Newton´s second law. Because the droplets originate from the gas phase it is assumed that the droplet velocity at the origin point is equal to the gas phase velocity. If a droplet trajectory crosses a wall the conclusion is drawn that the droplet is deposited on that wall. The droplet is then removed from the calculation. As mentioned above, the origin of a droplet is calculated using classical nucleation theory. As the droplets originate from the gas flow, it is assumed that the droplet velocity at the formation point is equal to the gas velocity at that point. Once the droplet is exposed to an altered gas velocity, a force acts on the droplet. This force results from the flow around the droplet and is called aerodynamic drag force $\boldsymbol{F}_D$. Consequently, the droplet velocity $\boldsymbol{U}_d$ converges to the gas phase velocity $\bar{\boldsymbol{U}}_g$. On the other hand, the same force with a negative sign acts on the gas phase. The aerodynamic drag force $\boldsymbol{F}_D$ can be calculated with the non-dimensional drag coefficient C_D. In contrast to the drag calculation on a fixed sphere, the slip velocity between gas phase and droplet must be incorporated into the equations. Due to the small droplet diameter d_d being no larger than a few micrometers, the particle Reynolds number Re_d is well below 1,000. Thus, the functional relationship between the Reynolds number and the drag coefficient can be calculated using the Schiller-Naumann correlation [25]. In the case of condensation, the droplets are so small, that the flow around the droplets cannot be described using continuum mechanics. Hence, a correction of the drag coefficient is necessary in conjunction with the condensation calculation, as stated by Gyarmathy [2]. This correction was originally suggested by Cunningham [26]. All further drag force calculations are based on Eq. 1 with the corrected drag coefficient [2] given by Eq. 2 and the original Schiller-Naumann correlation [25] given by Eq. 3. In addition to the variables mentioned in Eqs. 1–2, ρ_g is the gas density and Kn is the Knudsen number.

$$\boldsymbol{F}_D = \frac{\pi}{8} \cdot d_d^2 \cdot \rho_g \cdot C_{D,Cun} \cdot \left(\bar{\boldsymbol{U}}_g - \boldsymbol{U}_d\right)\left|\bar{\boldsymbol{U}}_g - \boldsymbol{U}_d\right| \tag{1}$$

$$C_{D,Cun} = C_D \frac{1}{1 + 2.53Kn} \tag{2}$$

$$C_D = \frac{24}{Re_d}\left(1 + 0.15 Re_d^{0.687}\right) \tag{3}$$

As long as the gas phase velocity $\bar{\boldsymbol{U}}_g$ is directly taken from the solution of the Reynolds averaged Navier-Stokes equations, turbulent fluctuations are not incorporated in the droplet path calculation. This approach is used by Gerber [27], Dykas, and Wroblewski [28] as well as by Sasao et al. [29]. It can be considered state of the art against the background of condensation calculations. In particular, for cases where droplet deposition is not in the focus of investigation but on the change in the thermodynamic state, researchers trust in this procedure. However, if investigations focus on droplet deposition, results are not accurate enough if the influence of turbulence fluctuations is not incorporated in droplet calculations. The need for an improved model in the context of condensation calculations in turbines is obviously clear from the conclusion of Starzmann et al. [30]: '*…further work on the problematic of droplet deposition is needed and a next step should be to implement more sophisticated treatments in 3D-CFD codes to verify the accuracy of the presented results*'.

A general insight on deposition mechanism is given by

experimental investigations in straight tubes flooded with a particle-laden gas. The obtained values are converted into non-dimensional values. Thereby, results obtained at different Reynolds numbers can be compared. In this context, the Reynolds number is calculated with the gas velocity and the tube diameter. The non-dimensional values are the deposition rate G_{dep+} (Eq. 4), defined for example by Wu and Young [31], and the non-dimensional particle relaxation time τ_+ (Eq. 5), used by Liu and Agarwal [32] as well as by Wu and Young [31]. In Eq. 4, the deposition rate G_{dep} is the mass flow of particles that are deposited on a surface divided by the area of the surface. The particle density ρ is the mass of particles divided by the gas volume. The friction velocity u_τ is calculated from the square root of the wall-shear stress divided by the gas density. The particle relaxation time τ_d is deduced from the force balance between inertia force and aerodynamic drag force on the assumption that Stokes' drag law is valid. A detailed derivation is given by Guha [10]. In Eq. 5, ν_g is the kinematic viscosity, ρ_d is the liquid density, and ρ_g is the gas density.

$$G_{dep+} = \frac{G_{dep}}{\rho \cdot u_\tau} \tag{4}$$

$$\tau_{d+} = \frac{\tau_d \cdot u_\tau^2}{\nu_g} = \frac{1}{18}\frac{\rho_d}{\rho_g}\left(\frac{d_d u_\tau}{\nu_g}\right)^2 \tag{5}$$

The results from droplet deposition experiments in straight tubes are shown in Fig. 1. Experimental results from Liu and Agarwal [32] as well as Sehmel [33] are plotted. CFD results are also shown to which chapter 1.3 refers to. It must be mentioned that the results from Sehmel shown in the figure are not directly noted in the original publication. Instead, the non-dimensional particle relaxation time and non-dimensional deposition rate are calculated from the values given in the publication. The non-dimensional deposition rate as a function of the non-dimensional relaxation time can be divided into three regimes. Thereby, in Fig. 1, the borders shown are taken from Wu and Young [31]. In regime 1, droplet deposition is mainly caused by diffusion, while in regime 3 the dominant effect is the large-scale turbulence structure. Finally, in regime 2, all sizes of turbulent fluctuations have an important role in the deposition process.

If the droplet path is calculated using Eq. 1, the turbulent fluctuation is not incorporated, nor is the diffusion process. In order to incorporate the turbulent fluctuation, the gas phase velocity $\bar{\boldsymbol{U}}_g$ resulting from Reynolds averaging must be replaced by the mean velocity $\bar{\boldsymbol{U}}_g$ plus the fluctuation velocity $\boldsymbol{U}'$. One way to handle this is by using direct numerical simulation (DNS). But summarizing this approach cannot be applied to the calculation of the flow in radial turbines due to the high computational effort. Large eddy simulation (LES) would reduce computational requirements but only give information about the large-scale turbulence. But LES give no benefit as in area 2, all scales have an impact on the deposition rate. Hence, the only practical way to handle deposition calculation in radial turbines is to deduce the fluctuation velocity from the turbulent kinetic energy k and the turbulent dissipation rate ε. The following approach is based on the work of Gosman and Ioannides [34]. A review is given in the publication of Guha [10].

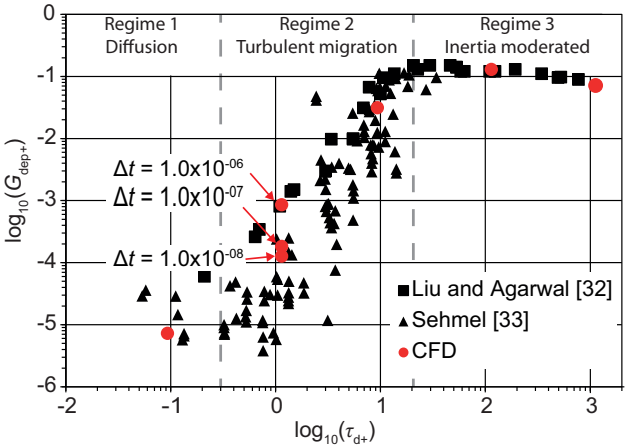

Figure 1. Deposition rate (Eq. 4) in a straight tube as a function of the non-dimensional relaxation time (Eq. 5)

A droplet enters a turbulence structure at a time t_0 and it is assumed that the droplet does not leave the structure before the structure disappears at time t_1. This means the force resulting from the fluctuation velocity of the turbulence structure acts on the droplet as long as the structure exists.

The turbulent fluctuation velocity is calculated using Eq. 6 from the turbulent kinetic energy k and a random number ξ. In contrast to the original publication a own random number is calculated for each coordinate. This fluctuation velocity is added to the mean velocity so that the turbulent fluctuation is incorporated in Eq. 1. Besides the fluctuation velocity, the time interval in which the turbulence structure exists is needed. This interval is calculated using Eq. 7. In this equation, l_e is the length of the structure calculated using Eq. 8, where c_μ is a turbulence model constant. The exponent applied to the turbulence model constant is different to the one used in the publication of Gosman and Ioannides [34] and is in accordance with the calculation of turbulence length scale in the used CFD code [35]. The random number ξ is calculated separately for each coordinate with the normal distribution (Eq. 9). ς is generated by a random number generator for equally distributed numbers between -0.5 and 0.5. If the standard deviation σ is set to 0.1, a good agreement is achieved between calculation and experiment, as will be shown in the validation. For different turbulence models different values might be necessary. In the future it might be desirable to use an advanced Reynolds Stress model in order to have a better prediction of the fluctuation velocity in wall normal direction.

$$\boldsymbol{U}' = \xi_{1\ldots3}\sqrt{\frac{2}{3}k} \tag{6}$$

$$\tau_e = \frac{l}{\sqrt{\frac{2}{3}k}} \tag{7}$$

$$l = \frac{c_\mu^{3/4} k^{3/2}}{\varepsilon},\ c_\mu = 0.09 \tag{8}$$

$$\xi = \begin{cases} \frac{1}{\sqrt{2\pi}\sigma}\exp\left[-\frac{1}{2}\left(\frac{\zeta}{\sigma}\right)^2\right] \text{if } \zeta \geq 0 \\ -\frac{1}{\sqrt{2\pi}\sigma}\exp\left[-\frac{1}{2}\left(\frac{\zeta}{\sigma}\right)^2\right] \text{if } \zeta < 0 \end{cases} \tag{9}$$

If the particles are very small the Brownian motion has a major impact on the deposition rate. Ounis, Ahmadi and McLaughlin [36] state that the Brownian motion becomes important for submicrometer-size particles: "*The Brownian motion significantly affects the dispersion of submicrometer-size particles near a wall.*". Wu and Young [31] mention that the diffusion process becomes important below a particle relaxation time of 0.3.

Therefore, the force $\boldsymbol{F}_B$, as a result of the Brownian motion, must be incorporated in the droplet path calculation. This force is calculated using Eq. 10, which is given by Guha [10] and is based on the publication of Ounis, Ahmadi and McLaughlin [37]. In this equation, k_B is the Boltzmann constant, T_g the temperature of the gas phase, D_B the diffusion coefficient, and Δt the integration time step. The diffusion coefficient D_B is calculated using Eq. 11. In addition to the previously mentioned variables, this equation includes the dynamic viscosity μ_g, the droplet diameter d_d, and the Cunningham correction factor C_C (Eq. 12). To be consistent with the publication of Guha [10], in the calculation, the Cunningham correction factor is taken from this publication and is slightly different to the one from Gyarmathy [2] used in Eq. 2.

$$\boldsymbol{F}_B = \xi_{1...3}\sqrt{\frac{2 \cdot k_B^2 \cdot T_g^2}{D_B \cdot \Delta t}} \tag{10}$$

$$D_B = \frac{k_B \cdot T_g}{3\pi \cdot \mu_g \cdot d_d} C_C \tag{11}$$

$$C_C = 1 + 2.7 \cdot Kn \tag{12}$$

There are other forces acting on the droplets that are incorporated in the calculation but have only a minor effect on the onset of deposition. Hence, only the literature where the equations to calculate this force can be found are given. Caused by a pressure gradient, the so-called pressure gradient force acts on a droplet (Lantermann [38]). A droplet in an inhomogeneous flow field is exposed to a lift force calculated based on the equation given by Sommerfeld [39]. A temperature gradient in a flow field results in the so-called thermophoretic force and is calculated using the equation published by Talbot et al. [40]. It must be mentioned that the influence of the thermophoretic force can get extraordinarily high if high temperature gradients exist in the flow. For example, Ryley and Davis [41] summarize that droplet deposition on steam turbine blades can be reduced by 30% to 90% if the blades are heated.

1.3 Validation tube

The experimental results of droplet deposition in straight tubes shown in Fig. 1 can be used for code validation. As the deposition rate is independent from the Reynolds number in the non-dimensional form of the diagram, the CFD boundary conditions must not fit the experimental ones. The Reynolds number in the CFD calculations is 6,500. The density of the gas is calculated using the state equations for ideal gases. The properties of the gas are: dynamic viscosity μ_g = 1.831 x 10^{-05} Pa·s; molar mass M = 28.96 g/mol. The outlet pressure is set to p = 1 bar. The temperature is constant at T_g = 20 °C. The diameter of the droplets d_d with a density of ρ_d = 997.0 kg/m³ is varied between 2 µm (τ_{d+} = 0.1) and 220 µm (τ_{d+} = 1000), and is constant from the inlet to the outlet. The deposition rate is determined in the second half part of the tube where the deposition rate is constant. The CFD results are shown additionally to the experimental results in Fig. 1. To ensure that the results are independent from the number of particle tracks calculated, in each calculation the number of tracks is doubled starting from an initial point. For the same reason, the integration time step is reduced by one magnitude from a starting point until an integration time step-independent solution is obtained. If τ_{d+} is greater than nine, an independent solution is obtained at 1,000 tracks and an integration time step of 1.0 x 10^{-6} s. For smaller relaxation times (τ_{d+} equal 1 and 0.1), 8,000 particle tracks and an integration time step of 1.0 x 10^{-7} s is necessary for an independent solution. For τ_{d+} = 1, the results of different time steps are shown in Fig. 1 to illustrate the influence of the integration time step. The CFD results are in satisfactory agreement with the experimental results. For the regime of turbulent migration and the regime inertia moderated this is achieved by setting the standard deviation σ to 0.1. For different turbulence models different values might be necessary.

2. RESULTS AND DISCUSSION

2.1 Radial turbine under investigation

A radial turbine is chosen for the investigations that is used for waste heat energy recovery in the process industry. The rotor blades are radially oriented at the leading edge. Figure 2 shows a meridional plot of the radial turbine under investigation with the reference planes and coordinates. The plane before the stator is marked with 0, the one before the impeller with 1, and the one after the impeller with 2. The axis of rotation is the z-axis. By convention, z is zero at the intersection point of hub and leading edge. All values of z are with regard to a value z_0. The radial position is marked with r/r_0. A part of the results will be shown as a function of S at different relative channel heights. By definition, the channel height is 0 % at the hub and 100 % at the casing. Results that are averaged in the circumferential direction and in the direction from hub to casing at constant S are shown as a

function of S_M. For a clear distinction between pressure side and suction side, in diagrams that are showing a meridional plot, the results obtained on the suction side are shown in the first quadrant of the coordinate system. Hence, the *z*-coordinate starts from zero to positive values. The through flow direction is from top left to bottom right. The results on the pressure side are shown in the second quadrant. The *z*-coordinate ranges from zero to negative values. The through flow is from top right to bottom left. Thus, Fig. 2 is showing the suction side. Besides, the meridional plot results are shown on S_1-surfaces, which are defined as surfaces at a constant relative channel height.

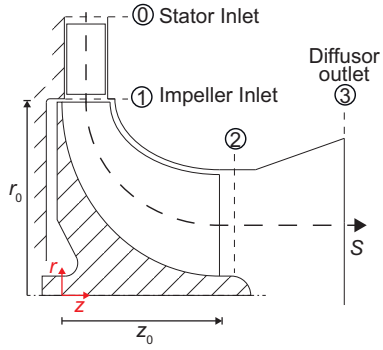

Figure 2. Sketch of the radial turbine

Total temperature and total pressure are specified as inlet boundary conditions before the stator in the CFD calculations. At the turbine outlet, the static pressure is specified. At all walls, the fluid has no slip and the walls are adiabatic. The fluid is a mixture of air and water steam defined as a two-component mixture. The absolute pressure is determined from the partial pressure of the two components. In each node of the computational mesh, the air temperature is equal to the water steam temperature. The air underlying the equation of the state of perfect gases has a molar mass of M = 28.96 g/mol with a constant isobaric heat capacity c_p = 1004.4 J/(kg·K), a constant dynamic viscosity μ_g = 1.831 x 10^{-05} Pa·s, and constant heat conductivity λ = 0.0261 W/(m·K). The water steam properties are calculated using the International Association for the Properties of Water and Steam (IAPWS) equations. The release IAPWS 97 is used. All equations and coefficients can be found in the available literature [42]. At the inlet, the mixture composition is specified and remains constant throughout the domain.

Figure 3 shows the radial turbine impeller. The hub and blade are shown in grey. A S_1-surface is plotted and coloured with the sub-cooling between 15 °C and 25 °C. Sub-cooling T_{sc} is defined as the saturation temperature T_{sat} minus the gas temperature T_g. A positive value means that the gas temperature is below the saturation temperature and, hence, that potential for the formation of droplets exists. The blue points give a qualitative impression of the locations of droplet deposition. The direction of the view is towards the rotor blade suction side. At the impeller inlet, sub-cooling is below 15 °C. In flow direction, the sub-cooling increases up to a value of approximately 25 °C. At this value, the condensation is high enough for a significant release of latent heat accompanied with a gas temperature increase and, hence, a reduction of sub-cooling. Once droplets have been formed, they might be deposited on the blade surfaces. The blue points show the locations where droplets are deposited. For the analysis of droplet deposition at a constant relative channel height, the location in the stream-wise direction at which deposition occurs first is marked. This is done at different channel heights and the connection of the determined points results in the red line shown in Fig. 3. To compare the location of maximum sub-cooling and the onset of deposition, the point of maximum sub-cooling is needed. This point is determined from surface streamlines on the S_1-surfaces. On each streamline, the location at which the sub-cooling has a local maximum is picked. The location of the streamline closest to the surface is used for further comparison in the meridional view. On the suction side, an uncertainty arises in the evaluation due to a secondary flow phenomenon. This can be seen in Fig. 3. Close to the suction surface, the sub-cooling first increases up to a value of 20 °C before dropping slightly (highlighted with a red oval). After that drop, the sub-cooling increases again before dropping down rapidly at a value of 25 °C (highlighted with a black oval). The first maximum is not caused by latent heat release. It is caused by transport of hotter gas from the hub to the casing.

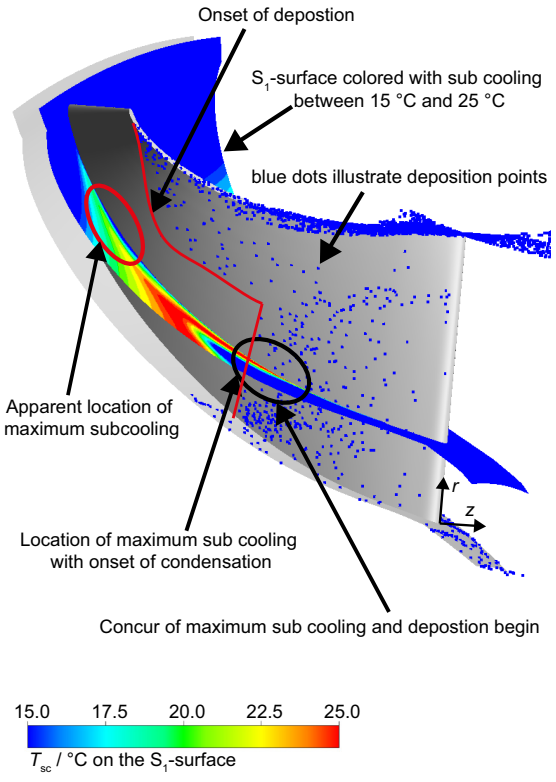

Figure 3. Sub-cooling in the impeller flow channel and droplet deposition at the impeller flow channel surfaces of the investigated radial turbine

Figure 4a/b show the results of the mesh independence study. In Fig. 4a the sub-cooling $T_{sc\text{-}sr}$, averaged in circumferential and in channel height direction with regard to a reference value, is plotted as a function of the stream-wise coordinate S_M for different mesh resolutions. The solution on the medium mesh can be called mesh-independent. The same is true for the droplet deposition on the pressure side, as

shown in Fig. 4b. The points plotted are the location at which first deposition takes place in the stream-wise direction at constant relative channel height. The grey full lines show the hub and casing. The dashed lines illustrate the rotor blade contour.

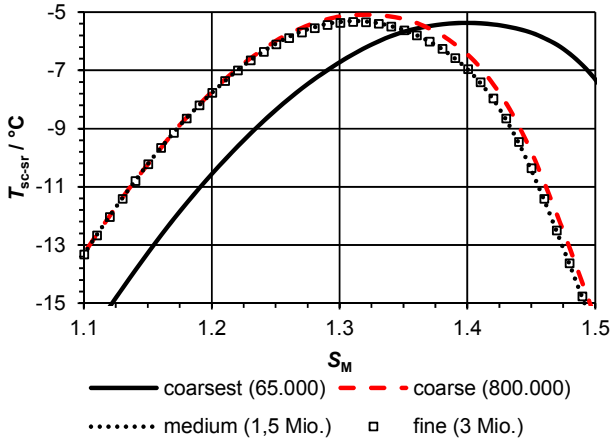

Figure 4a. Mesh independence study – sub-cooling in an extract of the impeller flow channel

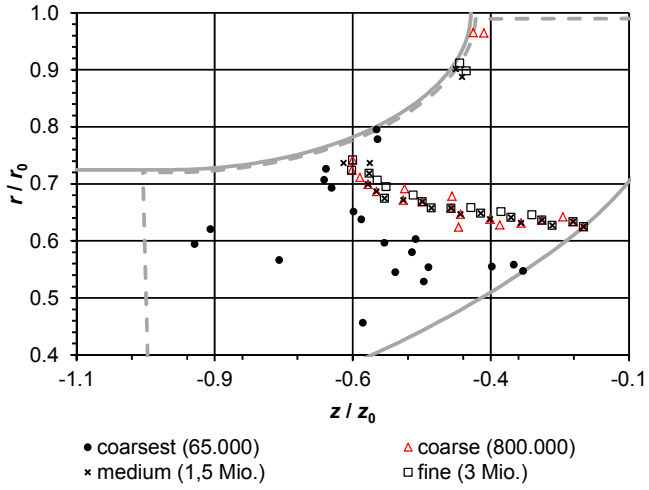

Figure 4b. Mesh independence study – deposition onset on the impeller blade pressure side surface

In Fig. 5, droplet deposition is shown incorporating all mentioned forces on the one hand and only the aerodynamic drag force calculated with the mean velocity on the other. The grey full lines enclose the part between stator-impeller gap, hub, and casing. The dashed lines illustrate the rotor blade contour. The pressure side is shown on the left and the suction side on the right. Results based on all mentioned forces are plotted using squares filled in red. The others are marked with red crosses. On the pressure side, a shift in deposition begin when incorporating all forces is clearly visible above 50 % relative channel height. But the difference between the two approaches is smaller at the hub. The reason for this is the higher blade curvature at the hub in comparison to the blade curvature at the casing. Hence, droplet deposition is dominated by inertia forces on a curved streamline at the hub, whereas it is dominated by turbulent migration and diffusion at the casing. On the suction side, no deposition occurs due to inertia on a curved stream line; hence, no data marked with crosses can be found on the suction side. However, deposition occurs due to diffusion and turbulent migration. The results clearly show the need to incorporate Brownian motion and turbulent fluctuation in the calculations.

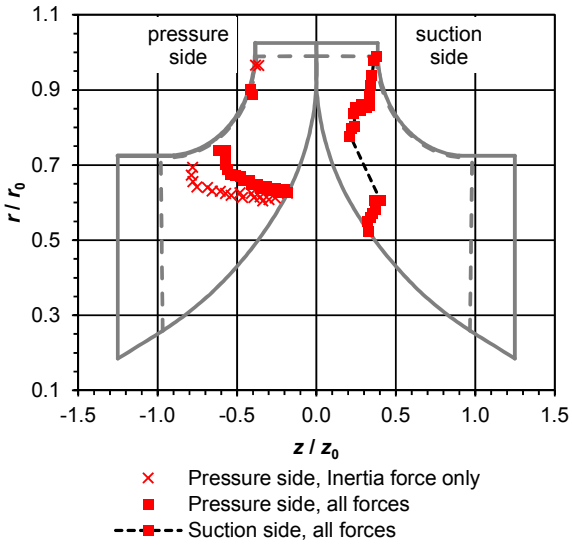

Figure 5. Influence of different droplet deposition mechanisms on the deposition onset on the impeller blade

Figure 3 provides an initial indication that a relationship between the locations of maximum sub-cooling and deposition start is present. Fig. 6, therefore, offers more detailed insight on the relation between both locations on the rotor blade pressure side. Three different calculations are performed using different inlet temperatures, where $T_{o\text{-}r}$ valued at zero is the design point temperature. With increasing inlet temperature, the location of maximum sub-cooling — shown using the black lines — is shifted in direction to the trailing edge. Up to a channel height of 90 %, the deposition begin — shown with the red symbols — is also shifted to the trailing edge with increasing inlet temperature. At above 90%, the deposition starts near the blade's leading edge. Droplets that are deposited there originate from the tip clearance flow.

Figure 7 shows the results on the suction side in the same manner as is shown in Fig. 6 for the pressure side. From the hub in direction to the casing, deposition starts at nearly constant stream-wise position first. Thereafter, droplet deposition is shifted to the leading edge. Qualitatively, the same is true for the location of maximum sub-cooling. The discrepancy between both locations on the suction side is caused by the secondary-flow phenomenon visible in Fig. 3. The relation between both locations shows a dependency on the coordinate *S*. While the location of maximum sub-cooling is near the leading edge, deposition starts before maximum sub-cooling is reached. On the other hand, if the location of maximum sub-cooling is near the trailing edge, deposition starts after maximum sub-cooling is reached. The reason is the increasing boundary layer thickness along the blade. As the thickness of the boundary layer increases, droplets have to travel a longer way from the nucleation point to the surface.

From the results it can be concluded that: If the interest is

in the onset of deposition in stream-wise direction, it is sufficient to calculate the line of maximum sub-cooling in steam-wise direction as this is in good accordance with the line of deposition onset in stream-wise direction.

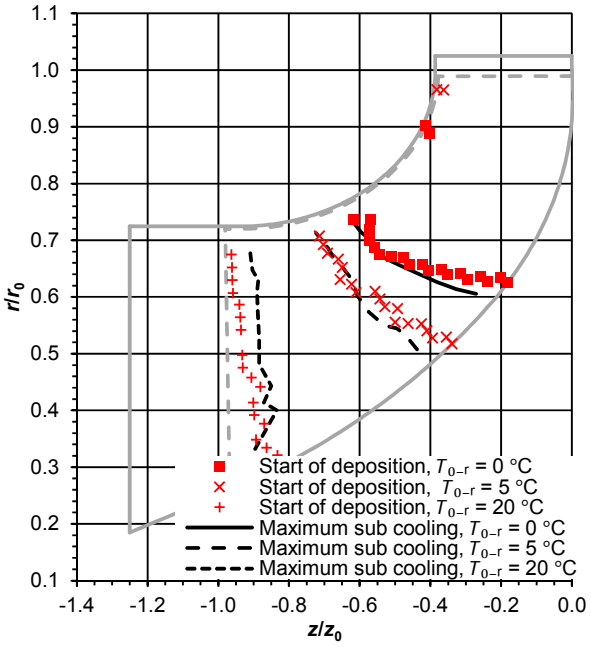

Figure 6. Droplet deposition and sub-cooling on the blade pressure side

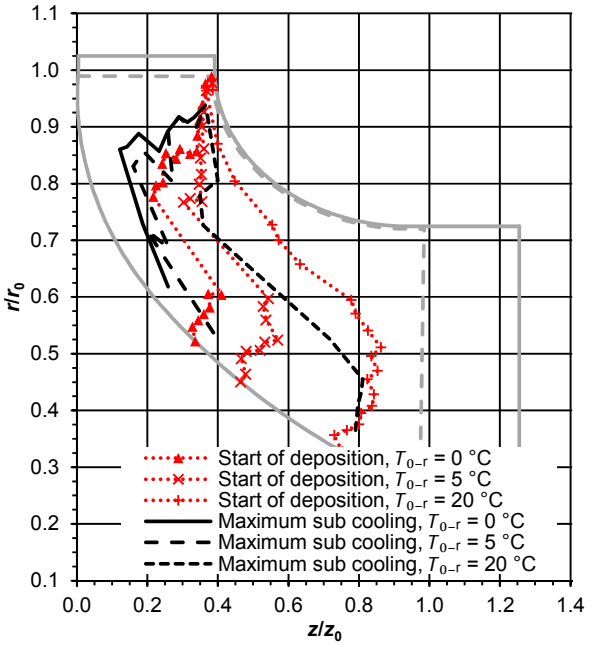

Figure 7. Droplet deposition and sub-cooling on the blade suction side

2.2 Influence of NRT on deposition calculation

As soon as steam undergoes sub-cooling, the potential for droplet formation exists. If the grade of sub-cooling is not sufficient, these droplets collapse in a little while. The macroscopic nucleation model used does not allow calculating the process of droplet collapse. Consequently, the formation and growth of droplets in even low sub-cooled steam will be calculated. However, the mass fraction of water droplets calculated in low sub-cooled steam is too small to have a noticeable influence on the temperature of the gas phase. Effectively, the macroscopic nucleation model gives the right results even though details are neglected. Nevertheless, the calculation of droplets in low sub-cooled vapour has an influence on the computing time. To speed up the CFD calculation, a threshold value *NRT* is specified, below which no droplets are initialized. This approach is also used by Gerber [43] and Fakhari [44]. The basic value is *NRT* = 1.0 x 10^{+15} 1/(m³·s) and is equal to that used by the previously mentioned authors. Lower threshold values should not have an influence on the sub-cooling as the additional droplets have no noticeable influence on the gas phase. Moreover, the sub-cooling course is the same for the basic value and a threshold value of 1.0 x 10^{+10} 1/(m³·s), as shown in Fig. 8. This figure shows the sub-cooling minus a reference value $T_{sc\text{-}sr}$ as a function of S_M in an averaged manner. The maximum sub-cooling value and its location are identical for both calculations; the same is true for the increase and drop of the graph. Obviously, the amount of droplets generated below a *NRT* of 1.0 x 10^{+15} 1/(m³·s) is to small to reduce the sub-cooling. The heat released from the droplets to the gas phase is not big enough for heating-up the gas phase.

Even though the threshold value has no influence on the sub-cooling, it might have an influence on the deposition. This influence is shown in Fig. 9. The figure shows the blade pressure side in meridional view. The surface is coloured with the deposition rate in a logarithmic manner. No deposition takes place in areas that are coloured in black. One can see that the deposition onset is shifted upstream if the threshold value is reduced from 1.0 x 10^{+15} 1/(m³·s) to 1.0 x 10^{+10} 1/(m³·s). In this additional area of deposition, the rate is six to 10 magnitudes lower than in the rest of the area. A further decrease of the threshold value leads, once again, to a shift in the upstream direction. The deposition rate in the new area is again several magnitudes lower. The results show that the influence of NRT is low for the deposition rate integrated over the surface but is high for the onset of deposition in stream wise direction.

In conclusion it can be said that the nucleation model is accurate enough to calculate the integrated deposition rate but must be improved to accurate and reliable calculate the deposition onset in stream-wise direction.

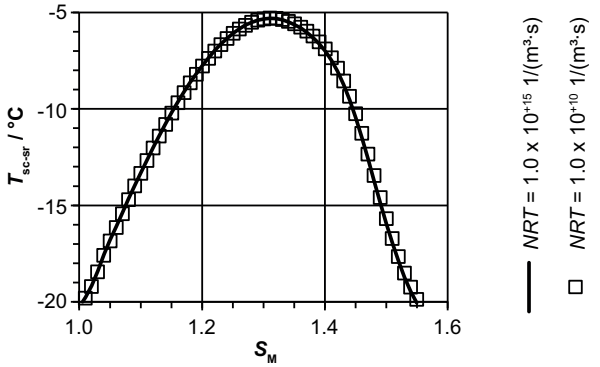

Figure 8. Influence of NRT on the sub-cooling in the impeller flow channel

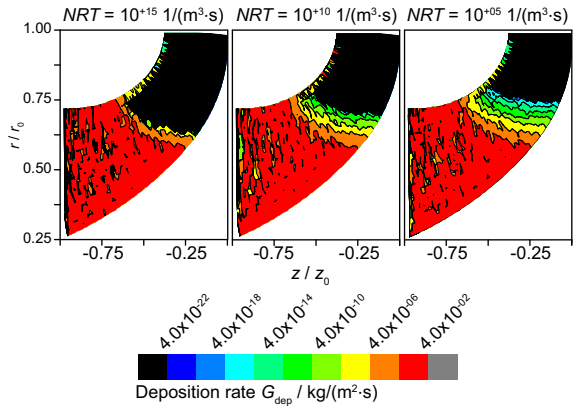

Figure 9. Deposition rate on the blade pressure side

2.3 Conclusions

Droplets in a broad diameter spectrum are deposited on the impeller blades of radial turbines when expanding a fluid below the saturation temperature. It is not sufficient to incorporate deposition due to inertia on a curved streamline alone. The influence of turbulent fluctuation and Brownian motion must be considered to predict the point of first deposition in a stream-wise direction to the right. For this calculation, a two-equation turbulence model can be used and the deposition calculation can be calibrated with the standard deviation.

With the used nucleation model and the widely accepted *NRT* value, it can be stated that deposition starts at the location of maximum sub-cooling. Consequently, the blade area that undergoes deposition is the area downstream of the line of maximum sub-cooling. In conclusion, it is not necessary to perform deposition calculations to determine the point of first droplet deposition in a stream-wise direction. It is sufficient to perform condensation calculations and determine the point of maximum sub-cooling.

Furthermore, the influence of *NRT* on the deposition is discussed. In conclusion, the position of deposition onset is shifted upstream when *NRT* gets smaller. Thereby, the deposition rate is reduced by several magnitudes. In a next step, two questions have to be answered. The first is a validation of the calculation. As mentioned, details of the nucleation process are not incorporated in the model. To estimate the correctness of the results, at first, condensation experiments in a Laval nozzle should be performed with simultaneous observation of the deposition. When the results are in line with the calculations of small *NRT*, then the next question must be answered: How do the small water portions behave?

REFERENCES

[1] Baumann, K. Recent developments in steam turbine practice. Journal of the Institution of Electrical Engineers. 1912, Vol. 48, 213.

[2] Gyarmathy, G. Grundlagen einer Theorie der Naßdampfturbine. Zürich: Juris, 1962.

[3] Bakhtar, F., Young, J. B., White, A. J. and Simpson, D. A. Classical nucleation theory and its application to condensing steam flow calculations. Proc. IMechE Part C: J. Mechanical Engineering Science. 2005, Vol. 219, 12, pp. 1315–1333.

[4] White, A. J. A comparison of modelling methods for polydispersed wet steam flow. International Journal for Numerical Methods in Engineering. 2003,Vol. 57, pp. 819–834.

[5] Yau, K. K. and Young, J. B. The deposition of fog droplets on steam turbine blades by turbulent diffusion. Journal of Turbomachinery. 1987, Vol. 109, 3, pp. 429–435.

[6] Young, J. B. and Yau, K. K. The inertial deposition of fog droplets on steam turbine blades. Journal of Turbomachinery. 1988, Vol. 110, 2, pp. 155–162.

[7] Crane, R. I. Droplet deposition in steam turbines. Proceedings of the Institution of Mechanical Engineers, Part C: Journal of Mechanical Engineering Science. 2004, Vol. 218, pp. 859–870

[8] Starzmann, J., Kaluza, P., Casey, M. V. and Sieverding, F. On kinematic relaxation and deposition of water droplets in the last stage of low-pressure steam turbines. Proceedings of the ASME Turbo Expo 2013: Power for Land, Sea and Air. 2013.

[9] Starzmann, J., Casey, M. V. and Mayer, J. F. Water droplet flow paths and droplet deposition in low-pressure steam turbines. High Performance Computing in Science and Engineering. 2013, Vol. 12, pp. 351–365

[10] Guha, A. Transport and deposition of particles in turbulent and laminar flow. Annu. Rev. Fluid Mech. 2008, Vol. 40, pp. 311–341.

[11] Young, J. B., Yau, K. K. and Walters, P. T. Fog droplet deposition and coarse water formation in low-pressure steam turbines: A combined experimental and theoretical analysis. Journal of Turbomachinery. 1988, Vol. 110, 2, pp. 163–172.

[12] Gomaa, H. and Weigand, B. Modelling and investigation of the interaction between drops and blades in compressor cascades with a droplet-laden inflow. Proceedings of the 14th International Symposium on Transport Phenomena and Dynamics of Rotating Machinery, ISROMAC—14. 2012.

[13] Schmehl, R., Rosskamp, H., Willmann, M. and Wittig, S. CFD analysis of spray propagation and evaporation including wall film formation and spray/film interactions. International Journal of Heat and Fluid Flow. 1999, Vol. 20, 5, pp. 520–529.

[14] Schuster, S., Benra, F. -K., Dohmen, H. J., König, S. and Martens, U. Sensitivity analysis of condensation model constant on calculated liquid film motion in radial turbines. Proceedings of the ASME Turbo Expo 2014: Power for Land, Sea and Air. 2014.

[15] Menter, F.R. Two-equation eddy-viscosity turbulence models for engineering applications. AIAA Journal. 1994, Vol. 32, 8.

[16] Crowe, C. T., Sharma, M. P. and Stock, D. E. Particle-source-in-cell (PSICELL) model for gas-droplet flows. Journal of Fluids Engineering, Transactions of the ASME. 1977, Vol. 99, 2, pp. 325–332.

[17] Gerber, A. G. and Kermani, M. J. A pressure-based Eulerian-Eulerian multi-phase model for non-equilibrium condensation in transonic steam flow. International Journal of Heat and Mass Transfer. 2004, Vol. 47, 10–11, pp. 2217–2231.

[18] Simpson, D. A. and White, A. J. Viscous and unsteady flow calculations of condensing steam in nozzles. International Journal of Heat and Fluid Flow. 2005, Vol. 26, 1, pp. 71–79.

[19] Yang, Y. and Shen, S. Numerical simulation on non-equilibrium spontaneous condensation in supersonic steam flow. International Communications in Heat and Mass Transfer. 2009, Vol. 36, 9, pp. 902–907.

[20] Wroblewski, W., Dykas, S. and Gepert, A. Steam condensing flow modeling in turbine channels. International Journal of Multiphase Flows. 2009, Vol. 35, 6, pp. 498–506.

[21] Patel, Y., Patel, G. and Turunen-Saaresti, T. The effect of turbulence and real gas models on the two-phase spontaneously condensing flow in nozzle. Proceedings of the ASME Turbo Expo 2013: Power for Land, Sea and Air. 2013.

[22] Moraga, F. J., Wang, L. and Ren, W. -M. Numerical sensitivity study and calibration of non-equilibrium wet steam model. Proceedings of the ASME Turbo Expo 2013: Power for Land, Sea and Air. 2013.

[23] Schuster, S., Benra, F. -K., Dohmen, H. J., König, S. and Martens, U. Influence of different gas models on the numerical results of high-velocity condensation. Conference on Modelling Fluid Flow (CMFF'12), Budapest, Hungary. 2012.

[24] Schuster, S., Benra, F. -K., Dohmen, H. J., König, S. and Martens, U. Investigation about the sensitivity of condensation calculations on model coefficients. Proceedings of the 15th International Symposium on Transport Phenomena and Dynamics of Rotating Machinery, ISROMAC—15. 2014.

[25] Schiller, L. and Naumann, A. Über die grundlegende Berechnung bei der Schwerkraftaufbereitung. Zeitschrift des Vereins Deutscher Ingenieure. 1933, Vol. 77, 12.

[26] Cunningham, E. On the velocity of steady fall of spherical particles through fluid medium. Proc R Soc A. 1910, Vol. 83.

[27] Gerber, A. G. Inhomogeneous multi-fluid model for prediction of non-equilibrium phase transition and droplet dynamics. Journal of Fluids Engineering. 2008, Vol. 130, 3.

[28] Dykas, S. and Wroblewski, W. Single- and two-fluid models for steam condensing flow modeling. International Journal of Multiphase Flow. 2011, Vol. 37, 9, pp. 1245–1253.

[29] Sasao, Y., Miyake, S., Okazaki, K., Yamamoto, S. and Ooyama, H. Eulerian-Lagrangian numerical simulation of wet steam flow through multi-stage steam turbine. Proceedings of the ASME Turbo Expo 2013: Power for Land, Sea and Air. 2013.

[30] Starzmann, J., Kaluza, P., Casey, M. V. and Sieverding, F. On kinematic relaxation and deposition of water droplets in the last stage of low-pressure steam turbines. Proceedings of the ASME Turbo Expo 2013: Power for Land, Sea and Air. 2013.

[31] Wu, Z. and Young, J. B. The deposition of small particles from a turbulent air flow in a curved duct. International Journal of Multiphase Flow. 2012, Vol. 44, pp. 34–47.

[32] Liu, B. Y. H. and Agarwal, J. K. Experimental observation of aerosol deposition in turbulent flow. Aerosol Science, Pergamon Press. 1974, Vol. 5, pp.145–155.

[33] Sehmel, G. A. Aerosol deposition from turbulent airstream in vertical conduits. AEC Research & Development Report. BNWL-578, 1968.

[34] Gosman, A. D. and Ioannides E.. Aspects of Computer Simulation of Liquid-Fueled Combustors. J. Energy, Vol 7, No. 6. 1983

[35] ANSYS®. CFX Academic Research, Release 12.1.

[36] Ounis H., Ahmadi G., and McLaughlin J. B.. Dispersion and Deposition of Brownian Particles from Point Sources in a Simulated Turbulent Channel Flow. Journal of Colloid and Interface Science, Vol. 147, No. 1. 1991

[37] Ounis H., Ahmadi G., and McLaughlin J. B.. Brownian Diffusion of Submicrometer Particles in the Viscous Sublayer, Journal of Colloid and Interface Science, Vol. 143, No. 1, 1991

[38] Lantermann, U. Simulation der Transport- and Depositionsvorgänge von Nanopartikeln in der Gasphase mittels Partikel-Monte-Carlo- and Lattice-Boltzmann-Methoden. s.l.: Dissertation, Universität Duisburg-Essen, p. 15, Eq. (2.37), 2006.

[39] Sommerfeld, M. Theoretical and Experimental Modelling of Particulate Flows. s.l.: von Karman Institute for Fluid Dynamics, Lecture Series 2000–06, p. 20, 2006.

[40] Talbot, L., Cheng, R. K., Schefer, R. W. and Willis, D. R. Thermophoresis of particles in a heated boundary layer. Journal of Fluid Mechanics. 1980, Vol. 101, 4, pp. 737–758.

[41] Ryley, D. J. and Davies, J. B. Effect of thermophoresis on fog droplet deposition on low-pressure steam turbine guide blades. Int. J. Heat & Fluid Flow. 1983, Vol. 4, 3, pp. 161–167.

[42] Wagner, W. and Kretzschmar, H. -J. International Steam Tables. Berlin Heidelberg: Springer, 2007.

[43] Gerber, A. G. Two-phase Eulerian/Lagrangian model for nucleating steam flow. Journal of Fluids Engineering. 2002, Vol. 124, 2, pp. 465–475.

[44] Fakhari, K. On the effects of unsteadiness on the condensation process in low-pressure steam turbines. Proceedings of the ASME Turbo Expo 2009: Power for Land, Sea and Air. 2009.